The ice-vapor interface during growth and sublimation

Maria Cascajo-Castresana[1,*], Sylvie Morin[1,2], Alexander M. Bittner[1,3]

[1] CIC nanoGUNE (BRTA), Av. Tolosa 76, 20018 Donostia-San Sebastián, ES-20018, Spain
[2] Department of Chemistry, York University, Toronto, ON M3J 1P3, Canada
[3] Ikerbasque Basque Foundation for Science, 48009 Bilbao, ES-48009, Spain

[*] Present Address: Tecnalia Research & Innovation, Paseo Mikeletegi 2, 20009 Donostia-San Sebastián, Spain

Correspondence to: Alexander M. Bittner (a.bittner@nanogune.eu)

Abstract. We employed Environmental Scanning Electron Microscopy (ESEM) in low humidity atmosphere to study the ice growth, coalescence of crystallites, polycrystalline film morphology and sublimation, in the temperature range of -10 ºC to -20 ºC. First, individual ice crystals grow in the shape of micron-sized hexagonal columns with stable basal faces. Their coalescence during further growth results in substantial surface defects and forms thick polycrystalline films, consisting of large grains separated by grain boundaries. The latter are composed of 1 to 3 µm wide pores, which are attributed to the coalescence of defective crystallite surfaces. Sublimation of isolated crystals and of films is defect-driven, and grain boundaries play a decisive role. A scallop-like concave structure forms, limited by sharp ridges, which are terminated by nanoscale asperities. The motivation for this work is also to evaluate ESEM's ability to provide a clean and reproducible environment for future study of nucleation and growth on atmospherically relevant nucleators such as materials of biological origin and inorganic materials. Hence, extensive information regarding potential ESEM beam damage and effect of impurities are discussed.

1 Introduction

Ice covers a much smaller area of our planet than liquid water. Some of this ice is subjected to large seasonal variations in temperature, giving rise to melting and sublimation. Understanding ice melting, flowing, sublimating and evaporating is key in understanding fully the impact of global warming. Here we focus exclusively on the study of ice/vapor interfaces, as present on snow, glaciers, permafrost soil, sea ice, and in clouds. Our low humidity conditions are of special relevance for sublimation at the poles and in Greenland, where ice sheets are in contact with air of low humidity, at temperatures well below those of

most glaciers on other continents (Bliss et al., 2011). The sublimation (and the redeposition) rate ultimately determine whether ice fields can exist at all.

The literature on ice growth and nucleation is vast, and well documented in recent reviews (Bailey and Hallett, 2004; Murphy and Koop, 2005; Libbrecht, 2005; Bartels-Rausch et al., 2012; Bartels-Rausch et al., 2014). It covers a broad spectrum of disciplines related to the study of geology, atmospheric science, and planetary science, but it is usually restricted to the macro- and millimeter scale.

Under some conditions, especially in clouds, small water droplets transform into small nearly spherical ice crystals with well rounded corners and edges. They are known as "droxtals", a term that combines the words droplet and crystal (Takahashi and Mori 2006, Gonda and Yamazaki 1978). While the shape can be reminiscent of shapes also found at the ice/vapor interface, droxtals formation require the presence of liquid water.

Ice growth from vapor requires that the water vapor reaches conditions of temperature T and water vapor pressure P_{water} for which water freezing and sublimation are at equilibrium. However, ice nuclei formation needs to overcome the activation nucleation barrier, through water vapor supersaturation. Once ice is formed, the solid/vapor interface of ice is subject to freezing (growth, deposition or desublimation) and sublimation (loss of water molecules), depending on temperature and pressure of the vapor phase. Summing up, the ice surface can grow when $P_{water}>P_{sat}$, and it will invariably lose material by sublimation when $P_{water}<P_{sat}$, where P_{sat} corresponds to the vapor pressure on the sublimation line of the phase diagram. We define the relative humidity h by

$$h = \frac{P_{\mathrm{water}}}{P_{\mathrm{sat}}} \quad (1)$$

This definition is valid for pure water vapor, but also for gas mixtures such as water vapor in air. Sublimation requires humidity values below 100%, while above 100%, i.e., at supersaturation, $P_{water}>P_{sat}$ results in ice growth via deposition (Kiselev et al., 2017). For ambient pressure (and hence slow diffusion in the gas phase), Lamb and Scott (Lamb and Scott, 2010) provide an overview of experiments and theories for ice growth from -30 ºC up to 0 ºC. However, by restricting the water vapor pressure below that of the triple point (611.7 Pa), which is 165 times lower than ambient pressure, conditions of very fast diffusion in the gas phase are achieved (compare also Sei and Gonda, 1989).

Our experimental conditions explore the range from -20°C to 0°C, at low water vapour pressure (i.e., below the triple point pressure of 611.7 Pa). Sei and Gonda (Sei and Gonda, 1989) provide details for growth in 40 Pa of air, at several % of supersaturation, altogether these conditions are comparable with that achievable in our ESEM. Their results nicely explain some of our data, especially the growth of high (long) hexagonal columns. Libbrecht discusses similar results (Libbrecht,

2004). It is also generally accepted that the growth velocity on the prism face is higher (this should result in plates) at -20 ºC < T < -10 ºC (Bailey and Hallett, 2009).

Why is the microstructure and its change during growth and coalescence (Nair et al., 2018) important? Grain boundaries show up, and in absence of impurities, typical microscale morphologies develop (Libbrecht, 2005; Sazaki et al., 2010; Asakawa et al., 2014; Kiselev et al., 2017), and rearrange (Krzyzak et al., 2007). Even supercooled water could exist (in highly curved nanoscale structures) (Nowak et al., 2008). In nature, impurities can concentrate in such defects (Baker et al., 2003; Bartels-Rausch et al., 2012; Bartels-Rausch, 2014), for example forming networks of water-filled microscale "veins", sometimes of relevance as habitat for organisms (Mader, 1992; Mader et al., 2006; Buford Price, 2000). Relevant structural details can already be observed on the nanoscale (Hondoh, 2009). This impurity effect has also been studied (or assumed to play a role) for micro- and nanoscale imaging (Cross, 1969; Cross, 1971; Mulvaney et al., 1988; Cullen and Baker, 2001; Rosenthal et al., 2007). Also, in this case, ions (from salts or acids) or dust particles in the crystals are thought to be the underlying cause for structures that develop during sublimation.

In this work, we modelled ice/vapor interfaces inside an Environmental Scanning Electron Microscope (ESEM), where temperature and humidity values can simulate conditions found in cold climates. Vapor freezing and ice sublimation give rise to micro- and nanoscale surface features that we characterize in detail. Freezing and sublimation depend on the microscopic ice morphology, and on its dynamical changes. We thus contribute microscopic evidence for relevant processes in atmospheric physics. While, we consider solely the solid/vapor interface, for temperatures well below the melting point, ice growth from vapor is not restricted to direct incorporation of molecules into the solid phase, it can also proceed via a supercooled liquid phase (Sei and Gonda, 1989), which can be extended (e.g. as droplet), or located at the ice surface as a "quasi-liquid layer".

The main goals of this work were to study ice morphologies, how they are attained from microcrystals, how isolated ice crystals and polycrystalline ice films form in real-time and sublime using ESEM (Kiselev et al., 2017; Ebert et al., 2002). Here we report all setup details, including the problematic control issues of temperature and pressure, beam damage on the nanoscale and on the microscale, and potential contamination issues. In addition, we wanted to evaluate ESEM's ability to provide a clean and reproducible environment for future study of nucleation and growth on atmospherically relevant nucleators such as materials of biological origin (Cascajo-Castresana et al., 2020) and inorganic materials.

2. Experimental Section

2.1 Environmental Scanning Electron Microscope (ESEM)

Images and movies of ice crystals during growth and sublimation on the wafer pieces were recorded in a FEG (Field Emission Gun) ESEM (Quanta 250, FEI), operated in the wet mode (Toth et al., 2003). The sample stage temperature was adjusted

between -10 ºC and -20 ºC by Peltier cooling. However, temperatures down to about -40 °C could be achievable, at least for small samples. Resistive heating allowed to reach ambient temperature quickly after the experimental runs. A thermocouple was located inside the Peltier stage, hence all temperature values are reported for readings at that location. The imaging gas was pure water vapor, introduced via an automated leak valve into the sample chamber. The vapor was produced from a heated reservoir of water (18 MOhm·cm, <5 ppb total organic content, Millipore), containing also a platinum wire for the catalytic decomposition of organic contaminants. The relative humidity in the chamber was controlled by increasing or decreasing the pressure P_{water} in small steps (< 5 Pa), in the range from ≈ 50 Pa up to ≈ 700 Pa.

Our beam voltage was set to values from 5 to 20 kV, the spot size was 3 to 5 (spot diameters ≈ 1 nm to 7 nm), and the aperture inside the column was kept at its smallest value, which reduces beam current and thus beam damage. The Supplement provides details on how to avoid beam damage, which can be mass loss (sublimation) or carbon deposition (from gas contamination) and melting (heating). In this way we avoided localized imaging artifacts.

Electron detection was achieved with the large field detector (LFD), placed some cm sideways (in the SEM images this is always the right-hand side), and away from the pole piece, or with the gaseous secondary electron detector GSED, a thin gold line, which encircled the pressure-limiting aperture. Standard settings were 1024 × 884 pixels with dwell times mainly of 10 to 30 µs for real-time images, and about ten times smaller for the fastest scans. For a beam current of 1.6 nA, applied to the smallest possible spot of 1 nm diameter, we obtain a maximal electron dose of 14000 e/s (Alonso et al., 2013).

The saturation water vapor pressure over ice, P_{sat}, was determined from the substrate temperature reading T in the ESEM, according to Murphy and Koop (Murphy and Koop, 2005):

$$P_{\mathrm{sat}}(T)/\mathrm{Pa} = \exp(9.550426 - 5723.265\mathrm{K}/T + 3.53068\ln(T/\mathrm{K}) - 0.00728332T/\mathrm{K}) \quad (2)$$

for $T > 110$ K. The humidity h is then simply the ratio of the measured pressure (which corresponds to P_{water}) and P_{sat}, see eq. (1). The technical details of our ESEM setup do not allow for stable $h > 1$ conditions. Any pressure (or temperature) adjustment to values in the P-T region of ice cause lowering of the pressure (pumping), or increase of temperature (heating of the sample), thus attaining the phase coexistence line at $h = 1$. This automatic pressure control balances water vapor supply and removal by pumping, and allows to reach $h > 1$ only for short times (at best some minutes). Due to the size of the specimen chamber, most of the vapor is at ≈+20 ºC, but due to the very small flow rate, it attains the substrate temperature when it approaches the Peltier stage/sample assembly.

Potential temperature gradients from Peltier stage to the substrate (see below) are very small; we verified that sublimation occurs at the correct temperature, when the pressure is lowered slowly (several Pa/min), and that first surface changes due to ice growth are observed at the same values when the pressure is increased even slower (1 Pa/min). Large pressure jumps (above

ca. 50 Pa) often result in a short loss of temperature control, due to sublimation or deposition of large amounts of ice. The pressure in the sample chamber is stable to at least 0.1 Pa (the pressure gauge gives values in Pa with three decimals). When we slowly increase the pressure at constant temperature, the ice growth was very fast (seconds) at $P_{water}>1.1P_{sat}$ (substantial supersaturation). Slow ice growth was observed exactly at $P_{water}=P_{sat}$. This requires waiting times in the range of minutes, as would be expected at equilibrium. From this observation we conclude that the pressure reading is exact, and we report values with one decimal. Although the pressure should read P=P0 at the onset of sublimation, this is harder to control for the instrument. We hypothesise that this is cause by a thick ice layer forming on cooled components of the sample holder. Here, we report simply the recorded data, translated into RH values.

2.2 Substrate

The experiments were carried out with a silica film grown on an n-doped silicon wafer. The silicon wafer ((111) orientation, thickness 0.27 mm, doped with phosphorus, resistivity 1 Ω cm) is cut in 4 × 4 mm^2 pieces by a wafer dicing saw (Disco DAD321). The pieces are thoroughly cleaned by sonication in an ultrasonicator (VWR Ultrasonic Cleaner) for 15 min in a sequence of three solvents: isopropanol (LC-MS chromasolv®, Sigma-Aldrich), acetone (ACS reagent >99.5%, Sigma-Aldrich), water (18 M Ω·cm, < 5 ppb total organic content, Millipore). They are blown dry with nitrogen and surface-oxidized in an oxygen plasma cleaner (Femto Diener) for approximately 8 min with a 10 sccm gas flow (10 Pa oxygen pressure). This surface treatment renders the wafers hydrophilic. For an experiment, liquid gallium-indium alloy is employed for bonding the wafer to a home-made copper stub. The stub is tightly fit into the Peltier stage by an aluminium foil spacer. For some experiments we used the surface of the copper stub, which is composed of copper oxide species.

3. Results and discussion

While clean flat oxidized silicon wafers (see Experimental Section) are typically used in our work, relatively rough copper surfaces (exposed to ambient air and thus oxidized) were also suitable substrate to grow ice. Both oxidized surfaces are amorphous. In our experiments, the pressure is adjusted to < 200 Pa ($h << 1$), then the substrate temperature is lowered from ambient to the desired ice growth temperature (≥ -20ºC). The pressure was then slowly increased until $h = 1$. The rate of ice growth can be controlled by controlling the humidity in the chamber, for example, fast growth can be achieved by pressure jumps to $h > 1$ (see Supplement), and stabilization at $h \leq 1$. The idea is to keep isobaric and isothermal conditions. However, small changes in sample temperature, which we carefully monitored, cannot be avoided. Subsequent sublimation requires $h < 1$, again accompanied by slight temperature changes.

In air, we would expect plate morphology between -20 ºC and -10 ºC under our low-pressure conditions (i.e. at fast gas phase diffusion), but only for $h >> 1$, at much slower gas phase diffusion, dendritic snowflake crystals (Gonda and Yamazaki, 1978;

Libbrecht, 2005; Takahashi and Mori, 2006; Bailey and Hallett, 2009). Between -10 ºC and -5°C, crystals can grow as columns or needles. We found for low supersaturation mainly hexagonal plates and columns from -20 °C to -10 °C (as discussed below). In accordance with Bailey and Hallett (Bailey and Hallett, 2004), individual crystals are of hexagonal geometry with facets of equal lengths as well as hexagonal scalene crystals, with three dissimilar facet lengths.

3.1 Early stages of growth

By increasing the water vapor pressure (by 10% - 20%) rapidly (in less than 5 s, see Supplement), the growth of individual hexagonal ice crystal is achieved on the oxidized silicon wafer, i.e. on an amorphous, OH-terminated silica surface. On the substrate, the orientation of ice crystals is random, with a few crystals having their c-axis perpendicular to the surface plane. The ice nucleation is progressive and homogeneous for the pressure and temperature conditions reported here. A characteristic example of ice morphology is given in **Figure 1A**, where randomly oriented isolated ice crystals are clearly visible, with a few features displaying highly defective crystal aggregates. These aggregates originate from the merging of nearby crystallites. The bright ridges in the image are usual for SEM (Castle and Zhdan, 1997; Nair et al., 2018) and correspond to a locally high flux of secondary electrons, due to higher emission rates from surfaces that point towards the detector. This is also the case for the prism faces on the left of **Figure 1B**. This image also shows another typical effect, namely that flat surfaces appear to have a bright, but blurry rim, in the vicinity of sharp edges. This is due to negative charges, which accumulate preferentially at sharp edges and corners. ESEM reduces these charges but cannot eliminate them completely (Toth et al., 2003). In order to investigate the effect of charging on ice growth (and sublimation), these processes were studied with the beam focused (and scanning) and not focused on the areas of interest. We observed that the presence of the beam resulted in no morphological changes in the ice crystal or film features. However, when prolonged scanning with a high beam voltage beam damage and carbon deposition altered the growth and sublimation processes (see Supplement).

Our conditions result in slow growth rates where water molecules attach more readily to facets with high Miller indices, and ice growth is homogeneous on the prism faces, keeping the edges of crystals straight (Elbaum and Wettlaufer, 1993). **Figure 1B** shows a well-resolved hexagonal ice crystal with its basal plane (0001) oriented nearly parallel to the substrate. When the growth is monitored over time a growth rate of ≈ 100 nm/s is observed at -18.7 ºC and 127 Pa, hence at h = 1.09 (9% supersaturation). In this particular experiment, the growth direction was normal (90º) to the to the plane of the prism faces (for more details see Supplement). Our conditions can be readily compared with those employed in other ESEM studies but the growth rate reported vary substantially. For example, Pedersen et al. (Pedersen et al., 2011) reported 300 nm/s at -20ºC (h not given) and Kiselev et al. (Kiselev et al., 2017) reported 3000 nm/s at -22ºC (h = 1.18).

Comparison of growth rates with other studies is very difficult, for example, other ESEM studies were carried out at temperature at or below -30 ºC (Pfalzgraff et al., 2010; Magee et al., 2014) and were concerned with qualitatively different growth modes. Above -10 ºC, the growth rate is much higher, e.g., >10000 nm/s at -7º C and 450 Pa (Chen et al., 2017). This

is based on enhanced gas phase diffusion at the higher temperature, while the mean free path remains nearly unchanged (Pruppacher and Klett, 1978). Other experiments, especially optical microscopy, employ moist air up to ambient pressure. The relatively high pressure of nitrogen and oxygen reduces the mean free path in the gas phase, and thus alters the velocity distribution of the water molecules impacting the ice surface. In these studies, even lower growth rates were reported, which can yield different growth morphology, see for example Libbrecht and Rickerby (Libbrecht and Rickerby, 2013), where the very high growth rate at relatively high temperature is counterbalanced by diffusion in a much denser gas phase, i.e., resulting in a smaller mean free path (Pruppacher and Klett, 1978) (see Supplement). A better comparison is possible with ice growth in 40 Pa of (wet) air, reported by Sei and Gonda (Sei and Gonda, 1989), who find (macroscopic) results in very good agreement with the growth rate for the feature shown in **Figure 1B**.

Some of the crystals in **Figure 1A** also display rounding-off ("roughening") of their edges. Under our experimental conditions this is associated with partial sublimation of existing crystals (Nelson, 1998) followed by their regrowth. These features are consistently observed for our imaging conditions (see **Figure 1A, Figure 2,** see also Supplement). Further evidence will be provided in Section 3.4. Close examination of our data points to fluctuations in pressure due to pumping cycles during imaging. Here and in the remaining of the text we use "roughening" to describe the development of macroscopically smooth, rounded shape. This is a dynamical process of the ice surface (Maruyama, 2005; Krzyzak, 2007; Asakawa et al., 2014; Magee et al., 2014). It is based on the gradual disappearance of flat surfaces (Nelson, 1998). Such macroscopically smooth surfaces are made up of high-index faces, which sublimate more rapidly than low-index (basal and prism) faces. Hence, rough surfaces appear during sublimation. While roughening occurs during sublimation (see section 3.4 and 3.5) Figure S10 (Supplement) illustrates, how roughening can occur during a growth cycle due to loss of temperature control.

In Figure 2, the basal planes of crystals 1 and 2 have neither perpendicular nor parallel to the surface and correspond to a later stage of growth based on their relative sizes. Crystals 3 and 4 have basal planes oriented perpendicular to the surface, while the isolated crystal 5 has its basal plane nearly parallel to the surface plane. Each feature in Figure 2 is ultimately based on a columnar crystal, but growing at very variable angles from the wafer surface (see e.g. Figure S9 (Supplement)). Under our experimental conditions, i.e. forming ice from water vapour, the resulting morphology is not analogous to that of droxtals reported by Gonda and Yamazaki (Gonda and Yamazaki, 1978).

Pfalzgraff et al. (Pfalzgraff et al., 2010) found pyramidal facets and curved (termed by the authors as "conical non-facetted") surfaces associated with ice growth. Pyramidal facets were not found, consistent with our observations. Pfalzgraff et al. grew their ice crystals typically between -30 ºC and -45 ºC, and report growth rates as fast as 700 nm/s for the prism faces. They also used the onset of ice ablation as a function of temperature during a variable pressure SEM experiment to provide a way to relate the conditions in the SEM chamber to establish the frost point. Because pressure changes are reported as ratios of water vapor pressure at the ablation temperature over water vapor pressure at the cooling stage temperature, further comparison

with our experimental conditions is difficult, in contrast to ESEM studies at higher temperatures (Nair et al., 2018; Chen, 2017).

We measured local growth velocities at isolated and merging crystals shown in **Figure 3** (see Figure S2 in Supplement). For our set of parameters (moderate supersaturation) we obtain values up to 200 nm/s. The values can be separated into max 100 nm/s at the six edges of the basal plane, and 50 to 150 nm/s for some prism faces. Some edges, though, appear to be completely pinned, which is not due to contact with the substrate. However, some faces (e.g., the basal plane A1 in **Figure 3**) expand only very slowly at their edges, and practically not in the direction normal to the face (see A1 in Figure 3). Even then, the center of the basal plane is preserved, as seen in **Figure 4A**.

When two growing crystals merge on the substrate, their relative orientation is usually at an angle, and a grain boundary forms. In the top view, a single grain boundary is not visible. But upon contact with other crystals, a large amount of strain energy is formed on the grain boundary, resulting in the formation of many defects. Hence, a corrugated surface formed during growth would result from such defects (see **Figure 3B** and **3C**). These "avalanche" defects (Pedersen et al., 2011) are formed very fast and appear even hundreds of µm away from the area of contact between two crystals, i.e. from the original single straight grain boundary. The origin of the phenomenon is the mismatch of the structure found initially on A1 and B1 (see **Figure 3A** and **3B**, see also **Figure 1A**). Merging of ice crystals and formation of grain boundaries was also observed with ESEM, reported by Magee et al. (Magee et al., 2014) at much lower temperatures and pressures (below -20 ºC) and by Pedersen et al. (Pedersen et al., 2011) at very similar to our conditions of pressure and temperature. Pedersen et al. propose that an avalanche of dislocations can originate at the newly forming grain boundary (Pedersen et al., 2011). This is evidenced by the presence of highly corrugated features (see for example A2) in **Figures 3B-3D.** In addition, in the early stages of the defective film growth, macro-steps are formed (see **Figure 3D**).

Hence, our results are in agreement with well-known results at low pressures and at small supersaturation (Kiselev et al., 2017; Sei and Gonda, 1989). Higher pressures, i.e., admixture of air, could be an option for a high-pressure cell; higher supersaturations are a principal issue with these conditions are the fast growth rates and size of resulting features that are more suitable for optical microscopy.

3.2 Growth of polycrystalline ice films

Crystal aggregation yields morphologies that differ from the general morphology of isolated crystals, at least in the early stages of growth (see **Figure 1**). Merging of many isolated crystals (see **Figure 3** for an example of three crystallites) produces a polycrystalline surface (see **Figure 4A**, where some crystals have merged). Ultimately, even the basal planes merge with other crystals, many grain boundaries and dislocations are expected to form, and facets are no longer visible (**Figure 4B**). The formation of a continuous film of ice required at least tens of µm thick deposits. Such polycrystalline ice films show typical

dark bands, which are assigned to gaps developing at grain boundaries from the merging of adjacent grains. We will be referring to these areas as grooves. The grooves often meet and display Y-shapes (see **Figure 4B**). This is in agreement with Krausko et al. (Krausko et al., 2014) who froze liquid water inside the ESEM specimen chamber, but also performed ESEM studies of condensing water vapor (Nair et al., 2018; Chen et al., 2017). Grains can be nicely detected and assigned by EBDS (Montagnat et al., 2015), but measuring the depth of the grooves requires AFM. The typical groove depth range was found to be 0.05 μm to 0.5 μm (Krzyzak et al., 2007; Zepeda et al., 2001). In our films, we found groove depths of up to 10 μm (see Supplement) which could be due to different growth conditions, such as observation at a later stage of growth. The width of the grooves was 2 μm on average.

The grooves appearance is similar to that of veins in natural ice (Mader, 1992; Mader et al., 2006; Buford Price, 2000), and indeed our structures sometimes meet at angles around 120º (**Figure 4**). However, the veins are larger, filled by brine (salt water of low freezing point) and more frequently oriented at relative angles of 120º. This is because the large ice grains in nature grow and developed their shape more slowly.

3.3 Microscale "pores" inside the grooves

During our measurements on polycrystalline ice films, we observed features that appear as small circular dark spots, which we term "pores", aligned inside the grooves (which are not to be confused with “ice veins” (Mader, 1992,; Mader et al., 2006; Buford Price, 2000). Analogous features to our pores have been observed at ice/brine interfaces (Vetráková et al., 2019). The pores appear in ESEM as black dots (see **Figure 4**) of 1 to 3 μm in diameter, which corresponds to the width of the grain boundaries. Under the chosen imaging conditions, pores appear in all the grain boundaries in **Figure 4**, but they are not evenly distributed. These features are not due to beam damage (see our detailed discussion in the Supplement). Furthermore, under our experimental conditions it is unlikely that the pores are related to the veins reported in salt-contaminated ice (Mader, 1992,; Mader et al., 2006; Buford Price, 2000) (see introduction). It is the first time these features are reported for similar growth conditions.

We postulate that pores form when corrugated faces merge. An example of this can be seeing for a corrugated face merging with a flat one in **Figure 3B-3D**. (see face labelled A2), a complex scenario that forms the base for polycrystalline growth from coalescing crystallites. The corrugated surface would then result in a large number of pores. Their diameter along a given groove would be related to the height of the uneven features (**see Figure S4C**). The situation is more complex when two corrugated surfaces meet: Now curved grooves form, filled by pores (**Figure 4**). Occasionally observed larger holes (>10 μm size, see **Figure 4** for two characteristic examples) can originate from large defects produced when growing grains merge laterally, while their vertical growth rate is too fast to allow for large gaps between the grains to be filled. Similar, but much

smaller holes are known from epitaxial ice growth (Thürmer and Nie, 2013). The nanoscale morphology of the grooves is unknown, and beam damage precludes further analysis by ESEM (see Supplement).

3.4 Sublimation of isolated ice crystals

Sublimation is achieved by lowering the pressure by at least a few Pa to $h < 1$ (this can also work at readings of $h>1$ due to the issues discussed in the experimental section). In the absence of apparent defects such as dislocation and grooves, water molecules can detach more readily from crystal edges where the prism and basal faces meet, as well as from the prism faces. Sublimation of the crystal shown in **Figure 5A** does not proceed uniformly. Water detaches initially from the area near the edge of the top surface and a rough surface is created (see **Figures 5 A and 5B**). In **Figures 5B** and **5C**, ridges and protrusions are clearly visible and often appearing as bright high-contrast features (white) (see Gonda and Sei 1987 for analogous behavior observed by optical microscopy). This process extends to the prism faces and becomes more pronounced in **Figure 5C**. As the sublimation proceeds further, the ridges delimit concave features seen mainly on what is left of the prism faces. These contrast changes are intrinsic (Nair et al., 2018), i.e., not related to the detector performance, which would result in a change in brightness over the whole image. The shape of the basal plane is more or less retained throughout this process (**Figures 5A to D**). This hexagonal plate-like crystal shrank both in height and diameter after 7 min, and it completely disappeared in ≈ 13 min. The lateral sublimation rate was initially slow, 80 nm/s between **Figure 5B** and **Figure 5C**, but then increased rapidly, as the crystal top surface attained an irregular morphology (ridges and protrusions) and as the crystal thickness decreased. The estimated lateral sublimation rate between **Figure 5C** and **Figure 5D** is 200 nm/s. For our temperature range (-20 ºC to -10 ºC) and crystals of the order of 100 µm in diameter, complete sublimation is achieved over several min, as found by Nelson with optical microscopy (Nelson, 1998). This value depends on temperature and pressure; related observations on single crystals sublimation are documented at -45ºC (Pfalzgraff et al., 2010), but also in our parameter range (Cross, 1969; Magee et al., 2014). A similar sublimation scenario is observed for several crystals in close contact and proximity, except for the presence of corrugations (**Figure 5E**) giving rise to extensive ridges and scallop shapes formation as seen in **Figure 5F**. The formation of strings of bright dots on what is left of the grains is clearly visible in **Figure 5F**. The morphological changes observed during sublimation is in excellent agreement with that of others (Nair et al, 2018; Cross, 1969; Magee et al., 2014); including the typical ridge or scallop morphology seen in **Figures 5C** and **5F**.

Closer inspection, but carefully avoiding beam damage (see Supplement), reveals that the bright ridges are entirely composed of sub-µm features, aligned along edges or grooves. Baker et al. found similar features at much lower temperature (Baker et al., 2003), however, they show a relation between the appearance of these features and the presence of contamination (in natural ice samples). This impurity effect has been studied by several authors who suggest that ions (from salts or acids) or dust particles in the crystals may be the underlying cause for the macroscopic structures that develop during sublimation (Cross, 1969; Cross, 1971; Mulvaney et al., 1988; Cullen and Baker, 2001; Rosenthal et al., 2007). In contrast, we exclude contamination; the few particles we found would by far no suffice to decorate all ridges during sublimation (see Supplement).

Our bright ridges stem from localized high emission currents and must be linked to the above-mentioned asperities that appear during evaporation. We explain their presence not by contamination as in natural samples (Baker et al., 2003), but by the coexistence of concave "scallop"-like surfaces (Libbrecht, 2005) with convex asperities (Chen et al., 2017). The concave surfaces form by sublimation of faces of crystals (Libbrecht, 2005), the convex ones are the tip-like asperities at the ridges, which delimit the concave areas (their curvature radii can reach the nanoscale, see Supplement). Whenever we zoomed into details of the asperities, we observed artefacts from beam damage (e.g. melting); it is thus likely that the smallest features are in the range of the beam diameter (several nm). The presence of both concave and convex features during sublimation is well established (hollow ice crystals, Gonda and Sei 1987).

3.5 Sublimation of ice films

The principal features of the sublimation process of polycrystalline ice are very similar to the case of isolated crystals discussed above, as long as the parameters are not changed to much lower temperatures (Pfalzgraff, 2010; Magee et al., 2014). However, in our case, for rather flat ice crystallites (**Figure 4C**), separated by grooves (dark lines), sublimation first causes "etching" and a widening of the grooves (**Figure 6A** and **6B**). Following the theory by Barnes et al. (Barnes et al., 2003), the etching of grain boundaries and grooves by sublimation should create ever widening channels. The widening of the grooves during sublimation can be visualized by optical microscopy (Barnes et al., 2003). We followed the etching in real time at -10ºC, where the widening is in the range of mm/min, similar to findings by Chen et al. (Chen et al., 2017). The grooves simply move vertically, together with the evaporating ice surface. When the grain boundary plane is not exactly normal to the surface, the grooves no longer mark the initial boundary location, and also move laterally. As the sublimation proceeds further (from **Figures 6B** to **6C**) features reminiscent of isolated crystals appear (Nair et al., 2018; Cross, 1971; Chen et al., 2017). Quantification of this process is rather difficult. However, the rates of sublimation are of the order of hundreds of μm/min, which appears to compare well with several images shown by other authors under similar conditions of temperature and pressure (Nair et al., 2018; Chen et al., 2017).

As sublimation proceeds (see **Figures 6B to 6C**), the ice asperity density increases. In polycrystalline films, asperities form during sublimation at locations where grains were located (Thompson, 2000). Hence, this increase in asperities indicate an increase in ice grain density during the film sublimation. This is a common feature of a polycrystalline film formation for which the grain structure resulting from the nucleation, growth, and coalescence processes during the early stage of growth is retained at the near surface of the silicon wafer; and where through competitive growth, grains with preferred orientations are favoured as thickness increases. The result of the competitive growth is seen in the film morphology reported in Figure 6A at the onset of sublimation, where fewer larger grains are visible at the surface of the film. **Figure 6C** also shows that at the later stages of sublimation (t = 124 s) the groove contrast appears inverted, i.e. white, as for sublimation of an isolated crystal (see **Figure 5**). In the discussion of Figure 5, this phenomenon is synchronized with the appearance of sharp features.

The change of contrast in the ESEM image during sublimation of polycrystalline and isolated crystals can be explained by taking a closer look at the ice morphology during sublimation. **Figure 7A** to **7D** shows how tens of µm large ice features change during sublimation. The dark features corresponding to the grains are becoming concave during sublimation. These concave features are especially well imaged next to bare surface areas, similar to our findings for sublimation of isolated crystals. In the final stages of sublimation, where the substrate exerts some influence on the ice morphology, the features meet in sharp ridges and tips/asperities, with radii down to the nanometer range (similar to the features at evaporating brine (Yang et al., 2017)). The interaction with the solid substrate has some stabilizing effect on these features, which could be mechanical (immobilization), but also thermal (good heat conduction against beam damage). However, the sharp tips exist also on the ice surface, at -20 ºC and 100 Pa (**Figure 7 E and F**). The appearance of inverted contrast in **Figure 6C** indicates that these sharp features also develop without apparent interaction with the solid substrate.

A specific problem here, but also more general, is contamination. We exclude contamination, and possible pinning of ice asperities at contamination spots, by testing growth and sublimation on large scales (see Supplement). **Figure 7C** and **7D** show some examples, which are reminiscent of Cross' images for apparently thicker films (Cross, 1969; Cross, 1971). However, we have repeatedly found this morphology at up to -10°C, at much higher temperature than in Cross' work (his equilibrium pressure < 0.01 Pa translates to < -90 ºC). The smallest radii might be well below 100 nm, but beam heating effects (see Supplement) hinder a closer observation. Whatever the nanoscale structure might be, the very appearance of the needles/spikes requires that the curvature on the surface changes from predominantly convex on the grains (except the relatively small area of the grooves) to a large fraction of concave features, as also observed in various ice crystal habits (Libbrecht, 2005).

4. Conclusions

We investigated the growth and sublimation of isolated ice crystals (hexagonal plates or columns, and prisms), grown in random directions on oxidized silicon wafer, and of polycrystalline films, by real-time, *in situ* ESEM. We find that crystalline substrates are not required to grow isolated crystals, except if epitaxial orientation is sought. We present an analysis of the observed microscale surface morphology, including polycrystalline ice films. The observed growth scenarios are generally compatible with reports based on SEM studies (mainly at lower temperatures), with recent ESEM results, and with optical microscopy, which is usually carried out at ambient pressure.

Our spatial and temporal resolution revealed new details on dynamic phenomena during ice growth. Specifically, we demonstrate how merging of isolated crystals, the development of corrugated surfaces and of grooves, ultimately creates films with typical polycrystalline ice surfaces. We thus documented the transition from single crystal to polycrystalline morphologies

for the full scenario of vapor growth, i.e., from the initial nucleation over coalescence of crystallites, to the final smooth surface, which is dominated by grooves.

The appearance of small "pores" in grooves has to our knowledge not been documented before and are interpreted as interface of two corrugated merging crystallites having multiple imperfections at their surfaces. Their coalescence results in the formation of additional defects in the form of a string of dark "pores", each of only 1-3 μm diameter.

We characterized the evolution of the ice morphology at the micro- and nanoscale, by following the evolution of rather complex micropatterns towards a concave "scallop" morphology. Each structure is lined by sharp ridges, which are composed of nanoscale asperities. Through careful control experiments, we know that contamination plays a minor role in their formation, different from natural samples that contain salts.

Further experiments call for technical improvements to prevent beam damage especially since the nanostructures are prone to heating and thus melting. We suggest WetSTEM techniques, more sensitive detectors, and improved electron sources. A different issue is moving towards more realistic conditions for atmospheric and geoscience research. ESEM setups allow only for pure water vapor, but no additional gases. This limits investigation of environmentally relevant conditions, including air, and impurities. Furthermore, in practice, only small supersaturation is accessible, which means that solid/liquid interfaces are only accessible at rather low pressure, such that for example typical snow formation cannot be investigated. Local dosing of water vapor could be a simple alternative to achieve the required very high supersaturation, at least when highly dynamic growth scenarios are desired.

Further development of ESEM would afford more flexibility in experimental design and could include lower temperatures (down to -40 ºC) and improved pressure control. A challenge is accessing the water/ice phase transition at relatively high pressure, and generally reaching the extreme values of temperature and pressure, and fast cooling rates. Ambient pressure would require a pressure cell with much loss of resolution. Another possibility would be the addition of traces of ice nucleators such as minerals (Vetráková et al., 2019) or biogenic matter (Cascajo-Castresana et al., 2020), to research cloud nucleation and frost formation. An in-situ method such as the one proposed in our study would allow to observe changes in morphology, determine the role of defects as well as impurities in ice in real time. For example, the ESEM environment offers flexibility to approach brine-filled veins in ice (Vetráková et al., 2019). Moving towards mixtures, the interaction of carbon dioxide/water vapor with dry ice/water ice, relevant for the Martian atmosphere, can be in the range of an advanced instrument.

Author contributions

All authors designed the experiments, carried them out, evaluated the results and prepared the manuscript.

Competing interests

The authors declare no competing interests.

Data availability

Data repository York University under doi.org/10.5683/SP2/S2HBAR

Acknowledgments

We are indebted to C. Tollan, CIC nanogune, for technical help with the ESEM. We are grateful to Prof. H. Mader, Bristol University for discussions on ice veins. We thank Prof. A. Chuvilin, CIC nanoGUNE, for discussing beam damage and contrast mechanisms. We acknowledge funding from FEI (Eindhoven, NL), Elkartek 2015 and 2019 (Basque Government), the Spanish MINECO grants PID2019-104650GB and MAT2013-46006-R, Basque Government Grant Proyecto de Investigación PI2013-57, and from the Maria de Maeztu "Units of Excellence" Programme MDM-2016-0618 (MINECO). S.M. acknowledges York University and CIC nanoGUNE for their support during her sabbatical and subsequent visits.

References

Alonso, J. M., Górzny, M. L. & Bittner, A. M. The physics of tobacco mosaic virus and virus-based devices in biotechnology. *Trends Biotechnol.* **31,** 530–538, https://doi.org/10.1016/j.tibtech.2013.05.013, 2013.

Asakawa, H., Sazaki, G., Yokoyama, E., Nagashima, K., Nakatsubo, S. & Furukawa, Y. Roles of surface/volume diffusion in the growth kinetics of elementary spiral steps on ice basal faces grown from water vapor. *Cryst. Growth Des.* **14,** 3210–3220, https://doi.org/10.1021/cg4014653,2014.

Bailey, M. & Hallett, J. Growth Rates and Habits of Ice Crystals between -20 ºC and -70 ºC. *J. Atmos. Sci.* **61,** 514–544, https://doi.org/10.1175/1520-0469(2004)061<0514:GRAHOI>2.0.CO;2, 2004.

Bailey, M. P. & Hallett, J. A Comprehensive Habit Diagram for Atmospheric Ice Crystals: Confirmation from the Laboratory, AIRS II, and Other Field Studies. *J. Atmos. Sci.* **66,** 2888–2899 https://doi.org/10.1175/2009JAS2883.1, 2009.

Baker, I., Cullen, D. & Iliescu, D. The microstructural location of impurities in ice. *Can. J. Phys.* **81,** 1–9,

https://doi.org/10.1139/p03-030, 2003.

Barnes, P. R. F., Wolff, E. W., Mallard, D. C. & Mader, H. M. SEM studies of the morphology and chemistry of polar ice. *Microsc. Res. Tech.* **62,** 62–69, https://doi.org/10.1002/jemt.10385, 2003.

Bartels-Rausch, T., Bergeron, V., Cartwright, J.H.E., Escribano, R., Finney, J.L., Grothe, H., Gutiérrez, P.J., Haapala, J., Kuhs, W.F., Pettersson, J.B.C., Price, S.D., Sainz-Díaz, C.I., Stokes, D.J., Strazzulla, G., Thomson, E.S., Trinks, H. & Uras-Aytemiz, N. Ice structures, patterns, and processes: A view across the icefields. *Rev. Mod. Phys.* **84,** 885–944, https://doi.org/10.1103/RevModPhys.84.885, 2012.

Bartels-Rausch, T., Jacobi, H.-W., Kahan, T. F., Thomas, J. L., Thomson, E. S., Abbatt, J. P. D., Ammann, M., Blackford, J. R., Bluhm, H., Boxe, C., Domine, F., Frey, M. M., Gladich, I., Guzmán, M. I., Heger, D., Huthwelker, Th., Klán, P., Kuhs, W. F., Kuo, M. H., Maus, S., Moussa, S. G., McNeill, V. F., Newberg, J. T., Pettersson, J. B. C., Roeselová, M., & Sodeau, J. R.: A review of air–ice chemical and physical interactions (AICI): liquids, quasi-liquids, and solids in snow, Atmos. Chem. Phys., 14, 1587–1633, https://doi.org/10.5194/acp-14-1587-2014, 2014.

Bliss, A.K., Cuffey, K.M., & Kavanaugh, J.L. Sublimation and surface energy budget of Taylor Glacier, Antarctica, J. Glaciology, 57, 684-696, https://doi.org/10.3189/002214311797409767, 2011.

Buford Price, P., A habitat for psychrophiles in deep Antarctic ice. *Prog. Natl. Acad. Sci.* **97**, 1247-1251, https://doi.org/10.1073/pnas.97.3.1247, 2000.

Cascajo-Castresana, M., David, R.O., Iriarte-Alonso, M.A., Bittner, A.M., & Marcolli, C. Protein aggregates nucleate ice: the example of apoferritin, Atmos. Chem. Phys. Discuss. 20, 3291-3315, https://doi.org/10.5194/acp-20-3291-2020, 2020.

Castle, J. E. & Zhdan, P. A. Characterization of surface topography by SEM and SFM: problems and solutions. *J. Phys. D. Appl. Phys.* **30,** 722, https://doi.org/10.1088/0022-3727/30/5/004, 1997.

Chen, X., Shu, J. & Chen, Q. Abnormal gas-liquid-solid phase transition behaviour of water observed with in situ environmental SEM. *Sci. Rep.* **7,** 46680, https://doi.org/10.1038/srep46680, 2017.

Cross, J. D. Scanning Electron Microscopy of Evaporating Ice. *Science* **164,** 174–175, https://doi.org/10.1126/science.164.3876.174, 1969.

Cross, J. D. The effect of impurities on the structure of evaporating ice. *J. Glaciol.* **59,** 287-292,

https://doi.org/10.3189/S0022143000013241, 1971.

Cullen, D. & Baker, I. Observation of impurities in ice. *Microsc. Res. Tech.* **55,** 198–207, https://doi.org/10.1002/jemt.10000, 2001.

Ebert, M., Inerle-Hof, M. & Weinbruch, S. Environmental scanning electron microscopy as a new technique to determine the hygroscopic behaviour of individual aerosol particles. *Atmos. Environ.* **36,** 5909–5916, https://doi.org/10.1016/S1352-2310(02)00774-4, 2002.

Elbaum, M. & Wettlaufer, J. S. Relation of growth and equilibrium crystal shapes. *Phys. Rev. E* **48,** https://doi.org/10.1103/PhysRevE.48.3180, 1993.

Gonda, T. & Yamazaki, T. Morphology of ice droxtals frown from supercooled water droplets. *J. Cryst. Growth* **45,** 66–69, https://doi.org/10.1016/0022-0248(78)90416-5, 1978.

Gonda, T. & Sei, T. Evaporation form of ice crystals in subsaturated air and their evaporation mechanism. *Proc. NIPR Symp. Polar. Meteorol. Glaciol.* **1,** 113–121, https://doi.org/10.15094/00003529, 1987

Hondoh, T., An Overview of Microphysical Processes in Ice Sheets: Toward Nanoglaciology, *Low Temp. Sci. Suppl. Issue* **68**, 1-23,https://**hdl.handle.net/2115/45404,** 2009.

Kiselev, A., Bachmann, F., Pedevilla, P., Cox, S.J., Michaelides, A., Gerthsen, D. & Leisner, T. Active sites in heterogeneous ice nucleation - the example of K-rich feldspars. *Science* **355,** 367-371, https://doi.org/10.1126/science.aai8034, 2017.

Krausko, J., Runštuk, J., Neděla, V., Klán, P. & Heger, D. Observation of a brine layer on an ice surface with an environmental scanning electron microscope at higher pressures and temperatures. *Langmuir* **30,** 5441–5447, https://doi.org/10.1021/la500334e, 2014.

Krzyzak, M., Techmer, K., Faria, S., Genov, G. & Kuhs, W. Atomic force microscopy of rearranging ice surfaces, in "Physics and Chemistry of Ice", W.F. Kuhs, ed., RSC Publishing, https://doi.org/10.1039/9781847557773, 2007.

Lamb, D. & Scott, W. D. The Mechanism of Ice Crystal Growth and Habit Formation. *Journal of the Atmospheric Sciences* **31,** 570–580, https://doi.org/10.1175/1520-0469(1974)031%3C0570:TMOICG%3E2.0.CO;2, 1974.

Libbrecht, K.G. A Critical Look at Ice Crystal Growth Data. https://arxiv.org/abs/cond-mat/0411662, 2004.

Libbrecht, K.G. The physics of snow crystals. *Rep. Prog. Phys.* **68,** 855–895 http://dx.doi.org/10.1088/0034-4885/68/4/R03, 2005.

Libbrecht, K. G. & Rickerby, M. E. Measurements of surface attachment kinetics for faceted ice crystal growth. *J. Cryst. Growth* **377,** 1–8, http://dx.doi.org/10.1016/j.jcrysgro.2013.04.037, 2013.

Mader, H. M. Observations of the water-vein system in polycrystalline ice. *J. Glaciol.* **38,** 333–347, https://doi.org/10.3189/S0022143000002227, 1992.

Mader, H.M., Petitt, M.E., Wadham, J.L., Wolff, E.W. & Parkes, R.J. Subsurface ice as a microbial habitat. *Geology* **34**(3), 169-172, https://doi.org/10.1130/G22096.1, 2006.

Magee, N. B., Miller, A., Amaral, M. & Cumiskey, A. Mesoscopic surface roughness of ice crystals pervasive across a wide range of ice crystal conditions. *Atmos. Chem. Phys.* **14,** 12357–12371, https://doi.org/10.5194/acp-14-12357-2014, 2014.

Maruyama, M. Roughening transition of prism faces of ice crystals grown from melt under pressure. *J. Cryst. Growth* **275,** 598–605, https://doi.org/10.1016/j.jcrysgro.2004.11.432, 2005.

Montagnat, M., Chauve, T., Barou, F., Tommasi, A., Beausir, B. & Fressengeas, C. Analysis of Dynamic Recrystallization of Ice from EBSD Orientation Mapping. *Front. Earth Sci.* **3,** 81, https://doi.org/10.3389/feart.2015.00081, 2015.

Mulvaney, R., Wolff, E. W. & Oates, K. Sulphuric acid at grain boundaries in Antarctic ice. *Nature* **331,** 247–249, https://doi.org/10.1038/331247a0, 1988.

Murphy, D. M. & Koop, T. Review of the vapour pressures of ice and supercooled water for atmospheric applications. *Q. J. R. Meteorol. Soc.* **131,** 1539–1565 https://doi.org/10.1256/qj.04.94, 2005.

Nair, M,. Husmann, A., Cameron, R.E. & Best, S.M., In situ ESEM imaging of the vapor-pressure-dependent sublimation-induced morphology of ice. *Phys. Rev. Mat.* **2**, 040401, https://doi.org/10.1103/PhysRevMaterials.2.040401, 2018.

Nelson, J. Sublimation of ice crystals from the vapor. *J. Atmosph. Sci.* **55,** 910–919, https://doi.org/10.1175/1520-0469(1998)055%3C0910:SOIC%3E2.0.CO;2, 1998.

Nowak, D., Heuberger, M., Zäch, M. & Christenson, H.K. Thermodynamic and kinetic supercooling of liquid in a wedge pore. *J. Chem. Phys.* **129**, 154509, https://doi.org/10.1063/1.2996293, 2008.

Pedersen, C., Mihranyan, A. & Strømme, M. Surface transition on ice induced by the formation of a grain boundary. *PLoS One* **6,** https://doi.org/10.1371/journal.pone.0024373, 2011.

Pfalzgraff, W. C., Hulscher, R. M. & Neshyba, S. P. Scanning electron microscopy and molecular dynamics of surfaces of growing and ablating hexagonal ice crystals. *Atmos. Chem. Phys. Discuss.* **9,** 20739–20763, https://doi.org/10.5194/acp-10-2927-2010, 2010.

Pruppacher, H.R. & Klett, J.D., Microphysics of Clouds and Precipitation, Reidel Publishing, Dordrecht, https://doi.org/10.1007/978-94-009-9905-3, 1978.

Rosenthal, W., Saleta, J. & Dozier, J. Scanning electron microscopy of impurity structures in snow. *Cold Reg. Sci. Technol.* **47,** 80–89, https://doi.org/10.1016/j.coldregions.2006.08.006, 2007.

Sazaki, G., Zepeda, S., Nakatsubo, S., Yokoyama, E. & Furukawa, Y. Elementary steps at the surface of ice crystals visualized by advanced optical microscopy. *Proc. Natl. Acad. Sci.* **107,** 19702–7, https://doi.org/10.1073/pnas.1008866107, 2010.

Sei, T. & Gonda, T. The growth mechanism and the habit change of ice crystals growing from the vapor phase. *J. Cryst. Growth* **94,** 697–707 https://doi.org/10.1016/0022-0248(89)90094-8, 1989.

Takahashi, C. & Mori, M. Growth of snow crystals from frozen water droplets. *Atmos. Res.* **82,** 385–390, https://doi.org/10.1016/j.atmosres.2005.12.013, 2006.

Thompson, C. V. Structure evolution during processing of polycrystalline films. Annu. Rev. Mater. Sci. **30**, 159-190, https://doi.org/10.1146/annurev.matsci.30.1.159, 2000.

Thürmer, K. & Nie, S. Formation of hexagonal and cubic ice during low-temperature growth. *Proc. Natl. Acad. Sci. U. S. A.* **110,** 11757–11762, https://doi.org/10.1073/pnas.1303001110, 2013.

Toth, M., Thiel, B. L. & Donald, A. M. Interpretation of secondary electron images obtained using a low vacuum SEM. *Ultramicroscopy* **94,** 71–87, https://doi.org/10.1016/s0304-3991(02)00203-6, 2003.

Vetráková, Ľ., Neděla, V., Runštuk, J. & Heger, D. The morphology of ice and liquid brine in an environmental scanning electron microscope: a study of the freezing methods. *The Cryosphere* **13**, 2385-2405, https://doi.org/10.5194/tc-13-2385-2019, 2019.

Yang, X., Neděla, V., Runštuk, J., Ondrušková, G., Krausko, J., Vetráková, Ľ. & Heger, D. Evaporating brine from frost flowers with electron microscopy and implications for atmospheric chemistry and sea-salt aerosol formation. *Atmos. Chem. Phys.* **17**, 6291-6303, https://doi.org/10.5194/acp-17-6291-2017, 2017.

Zepeda, S., Yeh, Y. & Orme, C. A. Atomic force microscope chamber for in situ studies of ice. *Rev. Sci. Instrum.* **72,** 4159

https://doi.org/10.1063/1.1406933, 2001.

Figure captions

Figure 1. Ice growth examples recorded at 20 kV. (A) Isolated crystals grown on an oxidized silicon wafer substrate. Note that some grains have started to touch producing polycrystalline ice. ESEM imaging conditions: P = 135.1 Pa, T = -18.4 ºC, P_{sat} = 120.4 Pa, h = 1.12. (B) Individual hexagonal crystal of ice on a clean silicon wafer. The basal plane is nearly parallel to the substrate. The outer rim is bright, an effect that might indicate charging. ESEM imaging conditions: P = 127.1 Pa, T = -18.7 ºC, P_{sat} = 117.0 Pa, h = 1.09.

Figure 2. Ice crystals on an oxidized silicon wafer substrate, imaged at 5 kV during growth. Hexagonal-like pillar morphologies are clearly identifiable. Some crystals display round edges. ESEM imaging conditions: P = 148.1 Pa, T = -18.2 ºC, P_{sat} = 122.7 Pa, h = 1.21.

Figure 3. Isolated crystals merging during growth. As soon as the crystals touch, the planes in contact show polycrystalline topography with a large density of grooves. ESEM imaging conditions: (A), (B), (C) P = 130.2 Pa, T = -17.9 °C, P_{sat} = 126.2 Pa, h = 1.03; (D) P = 126.8 Pa, T = -18.3 °C, P_{sat} = 121.5 Pa, h = 1.04. The images show the same area of the sample.

Figure 4. (A) Hexagonal pillars of isolated crystals and polycrystalline ice films grown on an oxidized copper surface. ESEM imaging conditions: P = 135.1 Pa, T = -17.8 °C, P_{sat} = 127.4 Pa, h = 1.06. (B) Typical polycrystalline ice surface after growth and coalescence of the crystals on Si. The grains appear bright with typical shading effects. They are limited by 1 to 2 µm wide dark bands ("grooves"). Three grooves meet at angles of mainly 90º to 120º. Each groove consists of aligned pores of ≈ 1-3 µm in diameter. P = 438.4 Pa, T = -4.8 ºC, P_{sat} = 409.0 Pa, h = 1.07. (C) Polycrystalline ice surface during growth. Circular pores aligned along grooves. P = 287.3 Pa, T = -10.3 ºC, P_{sat} = 253.3 Pa, h = 1.13.

Figure 5. Sublimation sequence of hexagonal crystals. (A) to (D) shows the basal plane of an isolated crystal. ESEM conditions: (A) P = 180 Pa, T = -15.2 ºC, P_{sat} = 162.4 Pa, h = 1.11; (B) P = 139 Pa, T = -18.2 ºC, P_{sat} = 122.7 Pa, h = 1.13; (C) P = 123 Pa, T = -19.1 ºC, P_{sat} = 112.6 Pa, h = 1.09; and (D) P = 97 Pa, T = -20.1 ºC, P_{sat} = 102.4 Pa, h = 0.95. All images have the same scale (see C). The time elapsed since the onset of sublimation is given in each figure. (E) Merged crystals, -18.3 ºC, P = 126.8 Pa, P_{sat} = 121.5 Pa, h = 1.04 (F) The same area during the last stage before complete sublimation (6 min later). The bright grey background is the pure silicon wafer surface; all other features are ice crystals. Some facets are decorated with bright lines (strings of bright dots). ESEM imaging conditions: P = 130.6 Pa, T = -17.1 ºC, P_{sat} = 136.1 Pa, h = 0.96.

Figure 6. A thick polycrystalline ice film during sublimation. The grooves widen substantially. The last image appears to show contrast inversion of the grooves. ESEM imaging conditions: (A) P = 253.4 Pa, T = -10.2 ºC, P_{sat} = 255.5 Pa, h = 0.99; (B) P = 230.9 Pa,

T = -10.1 °C, P_{sat} = 257.8 Pa, h = 0.90; and (C) P = 232.8 Pa, T = -10.1 °C, P_{sat} = 257.8 Pa, h = 0.90. The time from the onset of sublimation is given in the figures. All images have the same scale (see A).

Figure 7. A thick polycrystalline ice film during sublimation. Shapes reminiscent of isolated crystals appear. In the final stage, needles/spikes develop. The smallest radii of such structures is below 10 nm. ESEM imaging conditions: (A) P = 137.0 Pa, T = -15.0°C, P_{sat} = 165.4 Pa, h = 0.83; (B) P = 147.3 Pa, T = -13.5 °C, P_{sat} = 189.8 Pa, h = 0.78; (C) P = 142.0 Pa, T = -12.1 °C, P_{sat} = 215.6 Pa, h = 0.66; and (D) P = 129.0 Pa, T = -9.7 °C, P_{sat} = 267.1 Pa, h = 0.48. The time from the onset of sublimation is given in the figures. All images have the same scale (see C). (E): -20 °C. The ice on the right hand side part is much thicker than on the left, and shows the typical concave "scallop" shape on the 10 µm scale. This is replicated also in the sub-µm scale. The ridges (white lines) and tips appear very bright due to the high local emission current. (F) Zoom into (E).

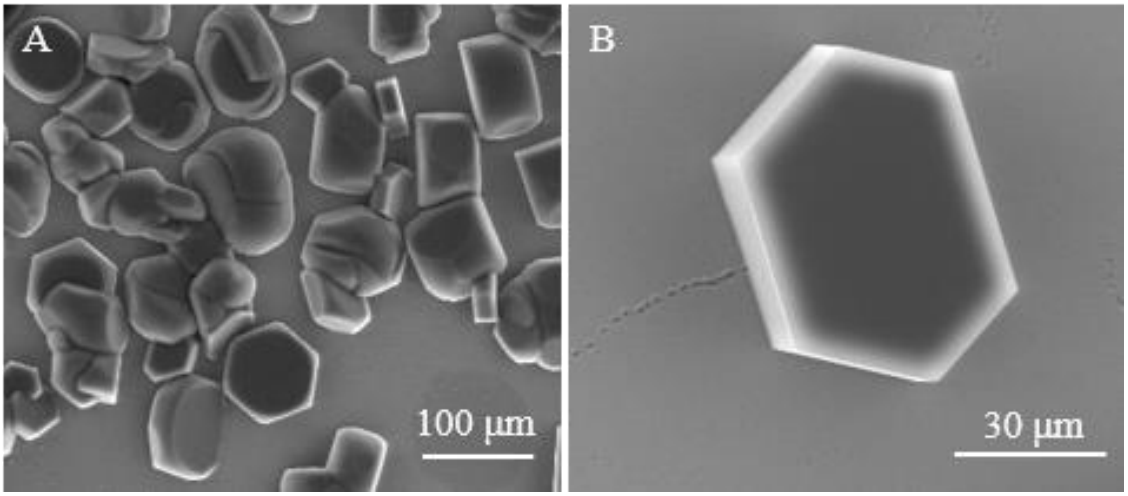

585 **Figure 1**

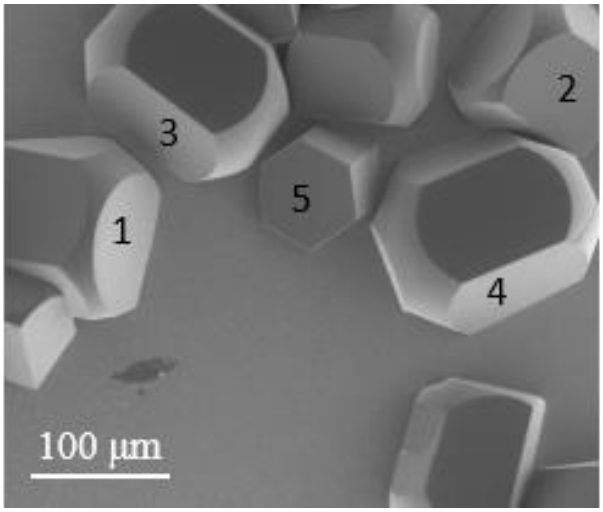

590 **Figure 2**

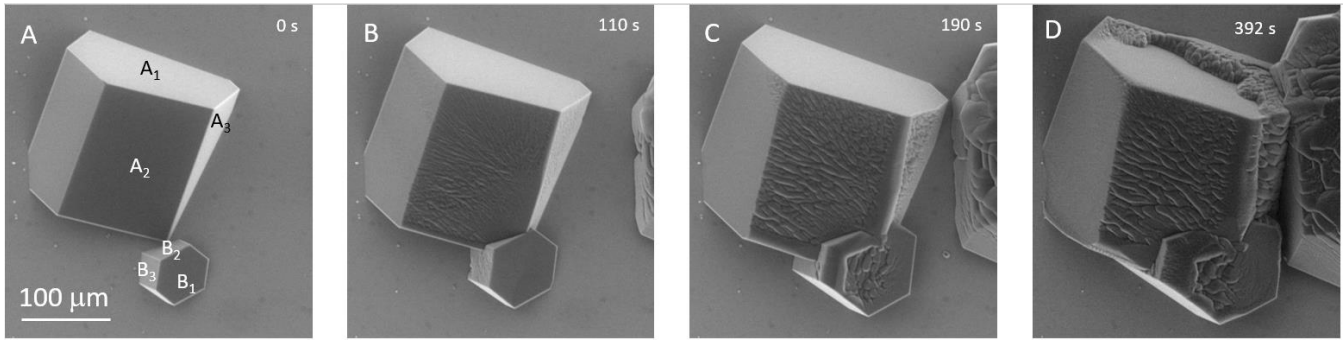

Figure 3

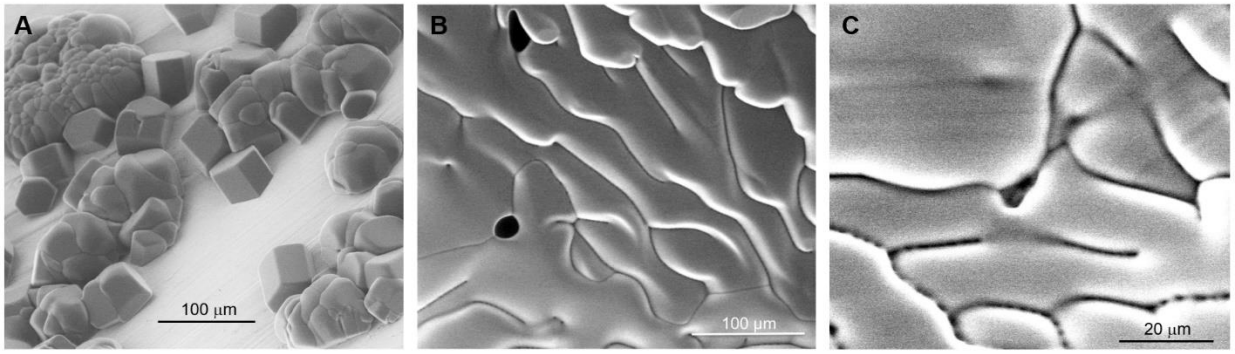

Figure 4

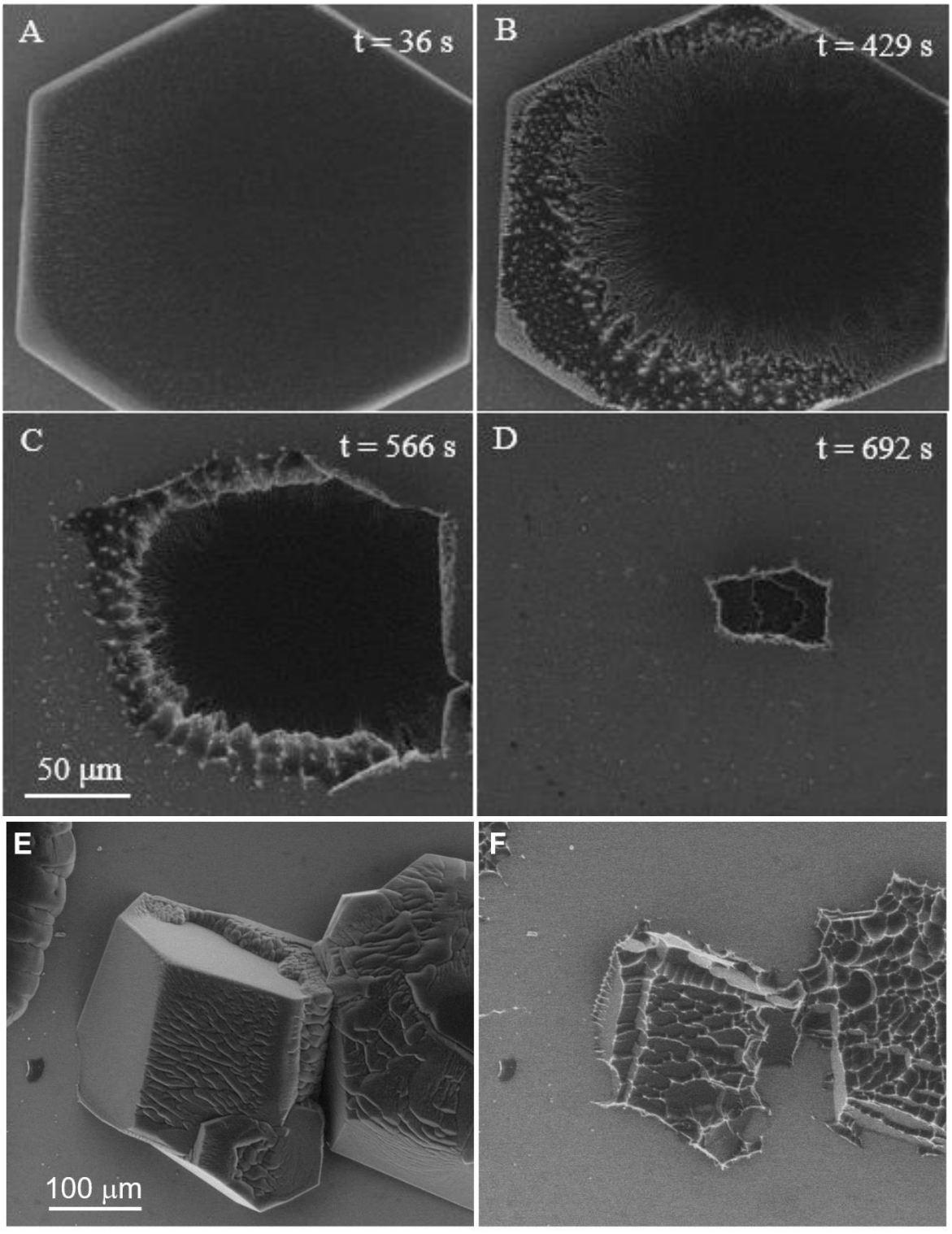

605 **Figure 5**

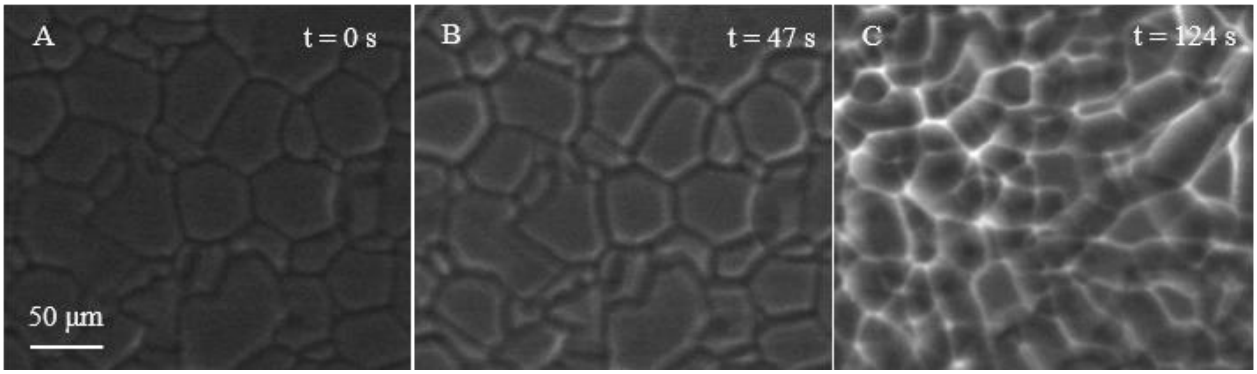

Figure 6

610

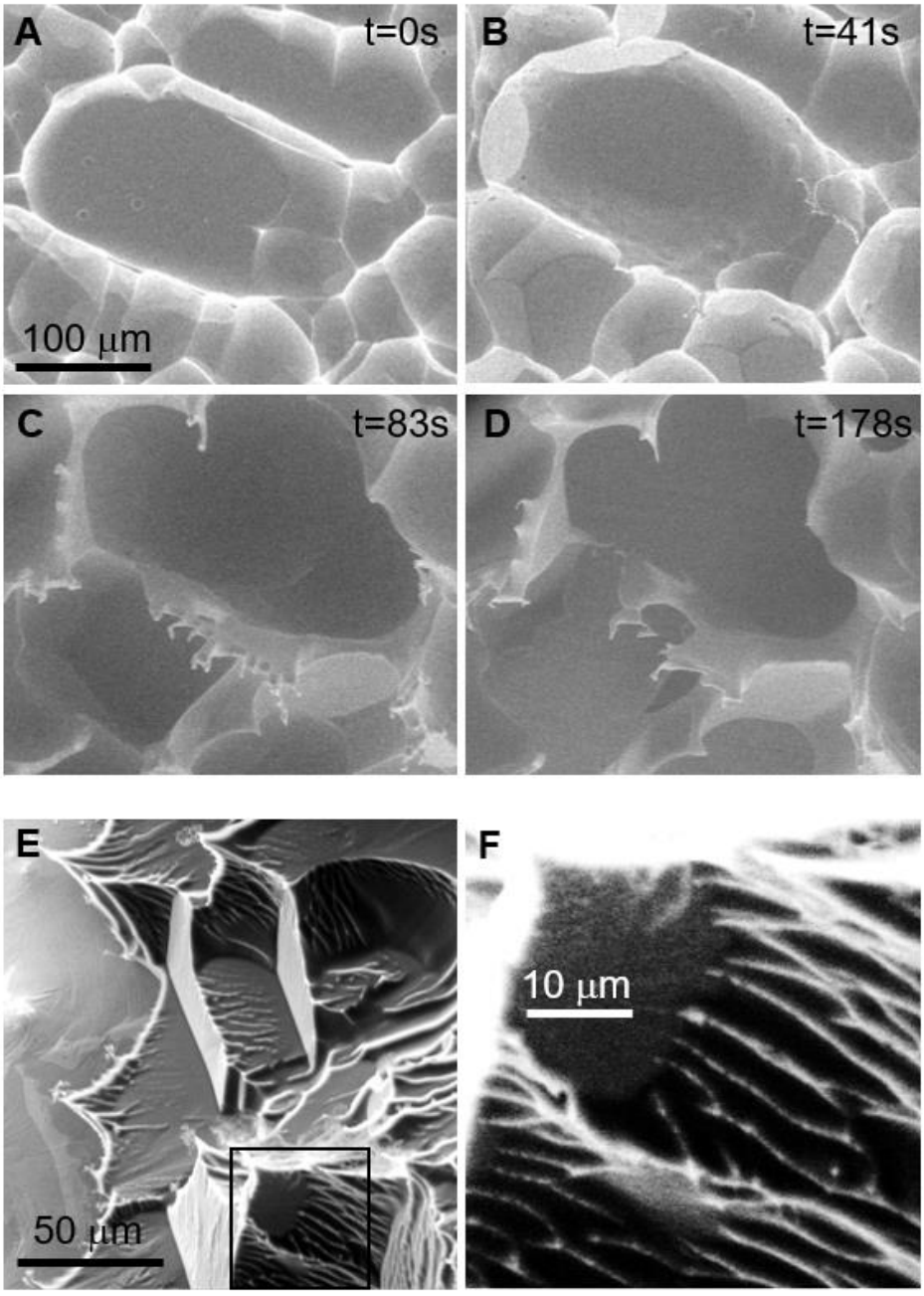

Figure 7

615

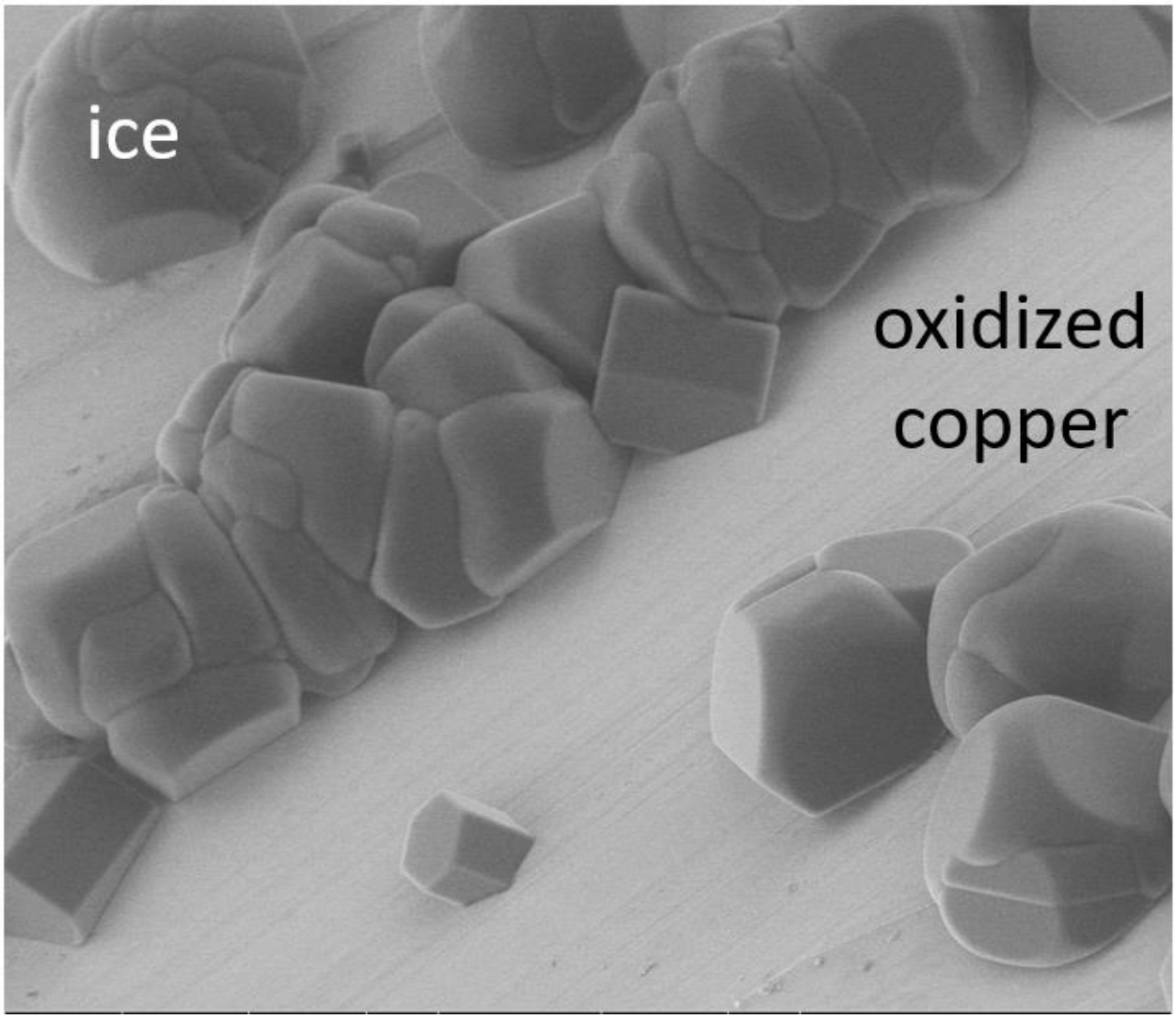

TOC (table of contents) figure